J. Fluid Mech. (2025), *vol.* 1017, A16, doi:10.1017/jfm.2025.10459

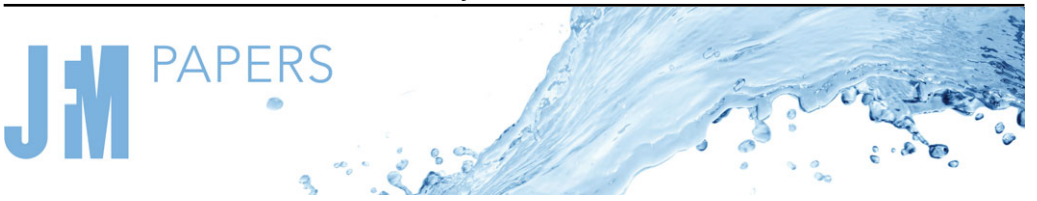

Surrounding fluid viscoelasticity reduces shear-induced gradient diffusivity of viscous drops

Anik Tarafder, Amirreza Rezaeepazhand and Kausik Sarkar

Department of Mechanical and Aerospace Engineering, The George Washington University, Washington, DC 20052, USA

Corresponding author: Kausik Sarkar, sarkar@gwu.edu

(Received 17 October 2024; revised 16 May 2025; accepted 2 July 2025)

Drops in a shear flow experience shear-induced diffusion due to drop–drop interactions. Here, the effects of medium viscoelasticity on shear-induced collective diffusivity are numerically investigated. A layer of viscous drops suspended in a viscoelastic fluid was simulated, fully resolving each deforming drop using a front-tracking method. The collective diffusivity is computed from the spreading of the drop layer with time, specifically a one-third scaling, as well as using an exponentially decaying dynamic structure factor of the system of drops. Both methods led to matching results. The surrounding viscoelasticity was shown to linearly reduce the diffusion-led spreading of the drop layer, the effect being stronger for less deformable drops (low capillary number). Because of the competition between the increasing effect with capillary number (Ca) and the decreasing effect with Weissenberg number (Wi), collective diffusivity vanishes at very low Ca and high enough Wi. The physics behind the hindering effects of viscoelasticity on shear-induced diffusion is explained with the help of drop–drop interactions in a viscoelastic fluid, where shear-induced interaction leads to trapping of drops into tumbling trajectories at lower Ca and higher Wi due to viscoelastic stresses. Using the simulated values, phenomenological correlations relating the shear-induced gradient diffusivity with Wi and Ca were found.

Key words: emulsions, drops, rheology

1. Introduction

Particles suspended in a shear flow experience diffusion because of irreversible hydrodynamic interactions between particles. This shear-induced diffusion plays a vital role in the rheology of a suspension or emulsion. It appears in two different forms.

In a suspension/emulsion, particles constantly interact with each other, and a tagged particle performs a random walk-like motion with its position varying with time as $\langle \boldsymbol{x} \cdot \boldsymbol{x} \rangle = 6D_s t$, D_s being the self-diffusivity (Acrivos 1995), which is present even in a uniformly mixed suspension or emulsion. Additionally, in the presence of a gradient of particle volume concentration ϕ, a smoothing of the gradient with a diffusive flux $-D_c \nabla \phi$ (D_c being gradient/collective diffusivity) occurs (Rallison & Hinch 1986; Grandchamp *et al.* 2013). The shear-induced diffusion is key to understanding enhanced mixing in process industries (Lopez & Graham 2008), lowering the effective viscosity and pressure drop in particle flow through a channel (Acrivos 1995), blunting of the velocity profile in a channel flow (Koh *et al.* 1994) and distribution of blood cells in vessels to produce a cell-free layer (Grandchamp *et al.* 2013). More recently, shear-induced diffusion has also been successful in effectively separating circulating tumour cells from blood using a microfluidic set-up (Zhou *et al.* 2018, Zhou & Papautsky 2019). Recently, we computed the shear-induced collective diffusivity in an emulsion of viscous drops in a viscous medium (Malipeddi & Sarkar, 2019*a*,*b*). Here, we compute the same in a viscoelastic medium.

Following the pioneering work of Eckstein *et al.* (1977) measuring self-diffusivity from the lateral displacement of individual particles in a Couette flow, many experimental and theoretical works have investigated various aspects of shear-induced diffusion in different flow conditions. A detailed review of previous work relating viscous suspension and emulsion can be found in our previous article (Malipeddi & Sarkar, 2019*a*,*b*). There were very few experimental measurements of shear-induced collective diffusion in viscous emulsions (King & Leighton 2001; Hudson 2003), which we discussed and successfully compared with in our previous article (Malipeddi & Sarkar, 2019*b*). Shear-induced diffusion depends on many factors such as particle properties – size, deformability, roughness, concentration, fluid properties – viscosity, density and viscoelasticity, as well as inertia and wall effects, as do single particle motion and particle interactions. Specifically, pair interactions between rigid smooth spheres in Stokes flow are reversible, i.e. two colliding spheres return to their original streamlines, requiring at least three particle interactions to break the symmetry (Marchioro & Acrivos 2001). The above symmetry is broken by one of many factors, such as deformability (Loewenberg & Hinch 1997), inertia (Kulkarni & Morris 2008), magnetic effects (Roure & Cunha 2018) or particle roughness (da Cunha and Hinch 1996). Note that, in a particle suspension, time reversibility is seen to be violated due to the chaotic nature of the dynamics (Marchioro & Acrivos 2001). Many of the earlier works have been devoted to understanding shear-induced diffusion of rigid particles in viscous suspensions. Only a few studies have reported rheological studies of viscoelastic emulsions (Zenit & Feng 2018). Recently, interest has grown in using the viscoelastic properties of a suspending fluid to focus targeted particles and cells in microchannels (Zhou & Papautsky 2020). The first normal stress difference and shear-dependent viscosity play critical roles in the effective focusing of particles in channels of different cross-sections. Fluid viscoelasticity results in the formation of chain-like structures of particles in shear flow that are absent in viscous flows (Won & Kim 2004; Scirocco, Vermant *et al.* 2004; Pasquino, Panariello *et al.* 2013) and promotes alignment of particles along the flow direction where the line joining three particles aligns along the flow direction (Choi & Hulsen 2012; Jaensson *et al.* 2016).

To our knowledge, there has not been a systematic study of the diffusion of deformable particles in viscoelastic emulsions. Kim *et al* (2000) repeated an earlier measurement of axial shear-induced gradient diffusion of rigid spheres in a viscous suspension by Leighton & Acrivos (1987) in a high molecular weight polymer (polyacrylamide) solution. They found that the diffusion decreased with the polymer concentration and the shear rate. Recently, we have shown that viscoelasticity has significant effects on drop trajectory

in pair interactions (Tarafder *et al.* 2022). The usual passing trajectories of a viscous system, where colliding drops slide past each other, change into tumbling ones in a viscoelastic system; collision traps them into a binary pair revolving around each other at low capillary and higher Weissenberg numbers. The tumbling trajectory results from the presence of a large region of spiralling streamlines around a single drop in a viscoelastic medium, helping trap the second approaching drop as well as the strong extensional stresses between drops in the separation quadrant of the collision. This study is motivated by the importance of such pair interactions on shear-induced diffusion. In this work, we numerically investigate the collective diffusion in a layer of concentrated viscous drops in shear at negligible inertia, extending our previous work in a viscous medium (Malipeddi & Sarkar, 2019*a*,*b*) to a viscoelastic medium with varying drop deformability and medium viscoelasticity. We note that the diffusivities are anisotropic. Similar to our previous studies, the system chosen here – a layer of drops homogenous in the flow and the vorticity directions in an unbounded shear – is suited to determining the collective diffusivity in the shear direction. In § 2, we describe the numerical procedure and discuss the results in § 3. Finally, we offer concluding remarks in § 4.

2. Mathematical formulation and numerical simulation

The dispersed continuous system is governed by the incompressible momentum conservation equations for velocity $\boldsymbol{u}$ in the entire domain Ω

$$\frac{\partial(\rho \mathbf{u})}{\partial t} + \nabla \cdot (\rho \mathbf{u}\mathbf{u}) = \boldsymbol{\nabla \cdot \tau} - \int_{\partial \boldsymbol{B}} \mathrm{d}x_{\boldsymbol{B}} \kappa \boldsymbol{n} \Gamma \delta(\boldsymbol{x} - \boldsymbol{x}_{\boldsymbol{B}}), \tag{2.1}$$

$$\boldsymbol{\nabla \cdot u} = 0. \tag{2.2}$$

The total stress $\boldsymbol{\tau}$ has pressure, viscoelastic and viscous parts

$$\boldsymbol{\tau} = -p\boldsymbol{I} + \boldsymbol{T}^p + \boldsymbol{T}^v, \quad \boldsymbol{T}^v = \mu_s \boldsymbol{D}, \tag{2.3}$$

where p is the pressure, μ_s is the solvent viscosity and $\boldsymbol{D} = (\boldsymbol{\nabla u}) + (\boldsymbol{\nabla u})^T$ is twice the deformation rate tensor. The superscript T represents the transpose and $\boldsymbol{T}^p$ is the viscoelastic stress due to the presence of polymer. In (2.1), ρ is the density, Γ is the surface tension (constant) along the drop surface ∂B consisting of $\boldsymbol{x}_B$ points, κ is the local curvature, $\boldsymbol{n}$ is the outward normal and $\delta(\boldsymbol{x} - \boldsymbol{x}_B)$ is the three-dimensional Dirac delta function. We use a modified Chilcott–Rallison-type (Chilcott & Rallison 1988; Matos *et al.* 2009) constitutive equation (also called the finite extensible nonlinear elastic modified Chilcott–Rallison or FENE-MCR) to model the viscoelasticity of the continuous phase. In our investigations of the effects of viscoelasticity, we have always chosen simple constitutive equations to explain the underlying physics. Unlike the Oldroyd-B equation used in our earlier studies (Aggarwal & Sarkar, 2007, 2008*a*,*b*; Mukherjee & Sarkar 2009, 2010), the FENE-MCR model in our recent studies (Mukherjee & Sarkar 2011, 2014) has a finite extensible viscosity; like Oldroyd-B, it has a constant shear viscosity. It has been extensively used in modelling different viscoelastic flows (Szabo *et al.* 1997; Ramaswamy & Leal 1999; Dou & Phan-Thien 2003; Kim *et al.* 2005). Furthermore, this constant viscosity viscoelastic model is applicable to a Boger fluid, which is also routinely used in experiments to investigate viscoelastic behaviours. e.g. for pair interactions between spheres in Boger fluids (Snijkers *et al.* 2013). Details of the implementation can be found in our previous work (Mukherjee *et al.* 2022; Tarafder *et al.* 2022). The viscoelastic stress

is determined by a simple rate type of equation,

$$\frac{\partial \boldsymbol{T}^p}{\partial t} + \left\{ \boldsymbol{u} \cdot \nabla \boldsymbol{T}^p - \nabla \boldsymbol{u} \cdot \boldsymbol{T}^p - \boldsymbol{T}^p \cdot \nabla \boldsymbol{u}^T \right\} + \frac{f}{\lambda} \boldsymbol{T}^p = \frac{f}{\lambda} \mu_p \boldsymbol{D}, \; f = \frac{L^2 + \dfrac{\lambda}{\mu_p} \left(\sum T_{ii}^p \right)}{L^2 - 3}. \tag{2.4}$$

Here, μ_p is the polymeric viscosity, λ the relaxation time and L the finite extensibility, introduced by the FENE-CR model, which limits the maximum length of the end-to-end vector for the polymer molecule. In the limit of $L \to \infty$ we obtain the Oldroyd-B equation with $f \to 1$ in (2.4). We use $L = 20$, increasing which was shown to make little difference to the results (Mukherjee & Sarkar 2013). We have provided additional details about the modified FENE-MCR model, noting that the nonlinearity does not affect the linear viscoelastic response, and results in a finite extensional viscosity and a constant shear viscosity (Oliveira 2003; Tarafder *et al.* 2022). In spite of its simplicity, we feel that the model is appropriate for the present purpose of explaining a phenomenon. However, note that shear thinning may qualitatively influence the problem of the particle dynamics in a viscoelastic medium. Studies of shear-induced string-like structure formation in a viscoelastic particulate flow have found no such structure in non-shear-thinning Boger fluids (Scirocco *et al.* 2004, Won & Kim 2004). Equations (2.1) and (2.2) along with the viscoelastic constitutive equation (2.4) are solved by a semi-implicit finite difference projection method in a Cartesian domain. An alternating direction implicit scheme is applied to ease the restriction on the time step. A multigrid method is used to solve the pressure position equation. A semi-analytic time integration method is used, which automatically achieves an elastic viscous stress splitting, alleviating some of the numerical stability issues common to viscoelastic numerical schemes (Sarkar & Schowalter 2000; Izbassarov & Muradoglu 2015). Details of the implementation of the above algorithm can be found in Li & Sarkar (2005), Aggarwal & Sarkar (2007) and Mukherjee & Sarkar (2013).

The simulation details for computing the shear-induced collective diffusivity are identical to our previous publications on viscous systems (Malipeddi & Sarkar 2019*a*,*b*, 2021). A total of $N = 70$ drops with radius a are placed in a random configuration in an initially compact layer at the middle (width $\sim 0.2\ L_y$) of the computational domain (figure 1) of size $L_y = 28a$ in the velocity gradient direction (y) and $L_x = L_z = 14a$ along the flow (x) and the vorticity (z) directions, leading to an initial volume fraction of $\sim$25 % in the compact layer. The independence of the result on domain dimensions, drop numbers and initial compact layer volume fractions (in the range of $\sim$25 %–43 %) has been investigated in a previous study of a viscous system (Malipeddi & Sarkar 2019*b*), indicating that the current configuration is sufficient for the simulation. Specifically, the domain length of $28a$ along the velocity gradient direction has been shown to be sufficient to neglect any wall effects (results differed negligibly from those obtained with a domain length of $42a$). Note that this approach differs from previous studies of hydrodynamic diffusivities (King & Leighton 2001; Hudson 2003), where drops uniformly distributed between walls experience competing effects of shear-induced diffusion and wall-induced migration. The computational domain is discretised with $96 \times 192 \times 96$ grid points ($\sim$14 grid points per drop diameter), which was shown to be sufficient in our earlier studies (Srivastava *et al.* 2016). The top and the bottom walls move with equal and opposite velocity U to obtain a shear rate $\dot{\gamma} = 2U/L_y$. Initially, the drops are placed in a fully developed shear flow (appropriate for Stokes flow) with no polymeric stresses. Periodic boundary conditions have been applied in the x and z-directions. The drop layer has a homogeneous distribution along the x and z directions. The drop radius a and the inverse

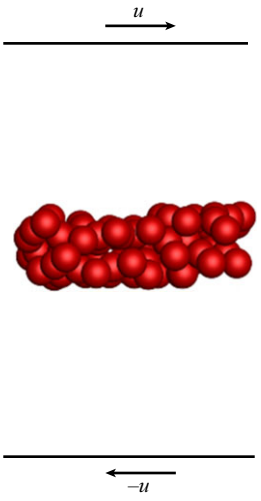

Figure 1. Schematic of the computational set-up.

shear rate $\dot{\gamma}^{-1}$ are used as the length and the time scales to define the Reynolds number $Re = \rho_m \dot{\gamma} a^2/\mu_m$, capillary number $Ca = \mu_m \dot{\gamma} a/$ and Weissenberg number $Wi = \lambda \dot{\gamma}$. The viscosity ratio $\lambda_\mu = \mu_d/\mu_m$ and the density ratio $\lambda_\rho = \rho_d/\rho_m$ have been kept at unity. The polymeric to total matrix viscosity ratio $\beta = \mu_{pm}/\mu_m$ is fixed at 0.5 (in Appendix, we briefly investigated the effects of β variation). Subscripts m and d denote fluid and drop phases, respectively. The total viscosity of the surrounding fluid μ_m comprises the polymeric and the solvent viscosities $\mu_m = \mu_{sm} + \mu_{pm}$. Because of the explicit nature of the code and thereby the diffusion limitation on time stepping, Re has been kept to 0.1 as a proxy for Stokes flow. We have previously shown it to be sufficient for matching with boundary element simulation of Stokes flow of viscous emulsions (Srivastava *et al.* 2016). Note that the front-tracking implementation is a smoothed-interface method, with the drop's surface moving with the local velocity interpolated from the Eulerian grid to the Lagrangian drop front, naturally avoiding interpenetration; no physical drop coalescence is considered. The above code was run with the help of George Washington University's High Performance Computing cluster PEGASUS.

The shear-induced collective diffusion of the drops in an unbounded shear (ensured by a large enough computational domain; see above) leads to a spreading of the initial layer of drops concentrated in the y-direction (homogeneous in the other two directions). It is governed by a coarse-grained one-dimensional diffusion equation for the drop volume fraction $\phi(y, t)$ (Hudson 2003)

$$\frac{\partial \phi}{\partial t'} = \frac{\partial}{\partial y'}\left(\frac{D^c_{yy}(\phi)}{\dot{\gamma} a^2}\frac{\partial \phi}{\partial y'}\right), \tag{2.5}$$

where $D^c_{yy} = \dot{\gamma}\phi a^2 f_2$ is the collective diffusivity coefficient, which is a function of local volume fraction $\phi(y, t)$ and f_2 is the non-dimensional collective diffusivity. The imposed unbounded shear here eliminates the advection term due to drop migration found in Hudson (2003). As has been discussed in detail in our previous article (Malipeddi & Sarkar, 2019*b*), the linear dependence of D^c_{yy} on the volume fraction ϕ is predicated on the dominance of the pairwise interactions validated *a posteriori* by the simulation results (also see Malipeddi & Sarkar, 2019*a*, 2021). We have shown that f_2 does not change with changing initial compact layer volume fraction (in the range of 25 %–43 %). Equation

(2.5) for a fixed number of particles spreading by diffusion yields a self-similar parabolic volume fraction (Grandchamp *et al.* 2013)

$$\psi\ (\eta) = \left(f_2 t'\right)^{1/3} \phi = \left(b - \eta^2/6\right), \qquad \eta = y'/\left(f_2 t'\right)^{1/3}, \tag{2.6}$$

with b as a free parameter, showing a 1/3rd scaling of the half-width $\underline{w}$ of the profile with time

$$\underline{w}^3 - \underline{w}_o^3 = K t', \qquad K = 9 f_2 N_0 / \left(4\sqrt{2}\right), \qquad N_0 = \int \phi\left(y', t'\right) \mathrm{d}y', \tag{2.7}$$

allowing determination of f_2. Here, $\underline{w}_o$ is the initial width and N_0 is a conserved quantity representing the number of drops diffusing out from a layer, calculated as $N_0 = NV/aL_xL_y$. Malipeddi & Sarkar (2019*b*) have identified an alternative half-width w computed from the drop positions y_i', $i = 1, \ldots, N$

$$w = \sqrt{\frac{1}{N}\sum_{i=1}^{N}\left(y_i' - \mu\right)^2}, \quad \mu = \frac{1}{N}\sum_{i=1}^{N} y_i'. \tag{2.8}$$

It can be related to the first moment of the analytical solution (2.6) leading to

$$w^3 - w_0^3 = K' t', \qquad K' = 9 f_2 N_0 / \left(10\sqrt{5}\right). \tag{2.9}$$

Using either expression for finding f_2 led to identical results within estimation uncertainties (Malipeddi & Sarkar, 2019*b*). However, the second method avoids the intermediate step of obtaining the coarse-grained volume fraction from the drop location. We plot $w^3 - w_0^3$ vs. $t'(= t\dot{\gamma})$ and calculate the slope to find the collective diffusivity. The simulations are run up to $t' \sim 180$ inverse shear unit times and $t' \leq t_0' = 20$ is discarded to make sure the drops are deformed and a linear region of $w^3 - w_0^3$ vs. t' is reached. Here, w_0 represents drop layer width at $t' = t_0'$. Similar to Malipeddi & Sarkar (2019*b*), the time evolution data excluding the initial transient are divided into smaller overlapping time intervals (∼80 non-dimensional times) with f_2 computed in each of them; their average is reported as an ensemble average with corresponding standard deviation as the uncertainty in its estimation. Previously, we have shown that f_2 does not depend on the initial volume fraction (in the range of ∼25 %–43 %) of the drop layer (Malipeddi & Sarkar, 2019*b*).

Shear-induced particle diffusivity, both self and gradient (or collective), can also be obtained from the dynamic structure factor (Rallison & Hinch 1986; Morris & Brady 1996; Marchioro & Acrivos 2001; Leshansky & Brady 2005, Leshansky *et al.* 2008). The dynamic structure factor has been useful for particle sizing in dynamic light scattering techniques, where the scattering of a monochromatic laser from the suspension volume is analysed to obtain the fluctuation autocorrelation. The exponential decay time of the autocorrelation is related to the diffusivity, which in turn is related to the particle size. Measurement of gradient diffusivity using the dynamic structure factor has previously been performed in homogeneous suspensions where the decay of spontaneously appearing fluctuation underlies the wavenumber or scale-dependent diffusivities. However, we have convincingly demonstrated that it can be used in a non-homogeneous system such as the centrally packed layer considered here to get useful information. It offered an excellent match with the diffusivity obtained by the continuum diffusion equation method (Malipeddi & Sarkar, 2019*a*,*b*, 2021). A detailed description of the method, including a discussion of the various issues arising from inhomogeneity of the system, has been given in Malipeddi and Sarkar (Malipeddi & Sarkar, 2019*a*). Briefly, the method is based on the particle autocorrelation function in the Fourier ($\boldsymbol{k}$ wavenumber) space of N drops located

at $\boldsymbol{x}'_\alpha(t'), \alpha = 1, 2, \ldots, N$

$$F\left(\boldsymbol{k}, t'\right) = \frac{1}{N}\left\langle \sum_{\alpha,\beta=1}^{N} e^{i\boldsymbol{k}\cdot\left(\boldsymbol{x}'_\alpha(t') - \boldsymbol{x}'_\beta(0)\right)}\right\rangle,$$
$$n\left(\boldsymbol{x}', t'\right) = \sum_{\alpha=1}^{N} \delta\left(\boldsymbol{x}' - \boldsymbol{x}'_\alpha\right), \qquad \hat{n}\left(\boldsymbol{k}, t'\right) = \sum_{\alpha=1}^{N} e^{i\boldsymbol{k}\cdot\boldsymbol{x}'_\alpha}. \tag{2.10}$$

It can be shown that the number density $n(\boldsymbol{x}', t')$ satisfies an advection-diffusion equation (Leshansky & Brady 2005)

$$\frac{\partial n}{\partial t} + \left(\boldsymbol{U} + \dot{\boldsymbol{\Gamma}} \cdot \boldsymbol{x}\right) \cdot \nabla n = \boldsymbol{D}^c \nabla^2 n \tag{2.11}$$

in a shear flow $\boldsymbol{U} + \dot{\boldsymbol{\Gamma}} \cdot \boldsymbol{x}$ ($\boldsymbol{U}$ is the average flow and $\dot{\boldsymbol{\Gamma}}$ is the velocity gradient tensor), with the diffusivity in the gradient direction being related to $F(\boldsymbol{k}, t')$ as

$$D^c_{yy} = -\frac{1}{k^2}\frac{\mathrm{d}\left(\ln F\right)}{\mathrm{d}t'}. \tag{2.12}$$

Note that, as noted in our previous publication (Malipeddi & Sarkar 2019*b*). the advection term in (2.11) does not affect the dynamics in a simple shear due to the orthogonality of the $\boldsymbol{k}$ ($= k\hat{\boldsymbol{y}}$) vector to the velocity field. We showed before that, even in this initially non-homogeneous system, the method can be applied to obtain a meaningful diffusivity D^c_{yy} in the limit of $k \to 0$ which can be matched with the results obtained from the continuum method described before. Note that, similar to the two different methods to compute f_2 described before, the autocorrelation can also be computed either directly from the particle positions (2.10) or using the coarse-grained volume fraction $\phi(y, t)$ satisfying the continuum (2.5). Both were shown to yield the same D^c_{yy} (Malipeddi & Sarkar 2019*b*). To compute $F(\boldsymbol{k}, t')$, signals for $t' < t_0$ are discarded and the rest are used to calculate the autocorrelation in 80 % overlapping intervals. They are averaged with the corresponding standard deviation used as an error of estimation. We will compare the gradient diffusivity represented by f_2 and D^c_{yy}.

3. Results

Previously, we offered a detailed comparison with the existing literature on hydrodynamic diffusivities for viscous systems (Malipeddi & Sarkar 2019*a*,*b*, 2021). Specifically, our computed collective diffusivity compared favourably with the experimental measurement (Hudson 2003; Malipeddy & Sarkar 2019*b*) found by the computed collective diffusivity matching with the zero capillary number limit of Ramachandran *et al* (2010) and it is 8–9 times higher than the self-diffusivity computed by Boundary Element Method simulations of Loewenberg and Hinch (1997), in conformity with the theoretical prediction of da Cunha and Hinch (1996). We are not aware of any studies of hydrodynamic shear direction collective diffusivities of drops in a viscoelastic medium. Specifically, figures 2 and 3 show snapshots of a layer of closed-packed drops spreading with time in the velocity gradient direction due to shear-induced diffusion. In figure 2, for $Ca = 0.2$, both $Wi = 0.0$ and 2.0 cases show that the drops spread in the shear direction due to diffusion, with the spreading being less for the higher Wi ($= 2.0$) case. We observe that, at the same time instant, drops are more deformed and inclined in the flow direction for $Wi = 2.0$ compared with $Wi = 0.0$, leading to less spreading of the layer for the more viscoelastic case. In our previous study of viscous emulsion, we noted that shear-induced collective diffusivity is a non-monotonic function of Ca due to the competing effects of increased drop deformation and stronger alignment with the flow at higher Ca. At a lower $Ca = 0.02$, decreased deformation leads to smaller diffusion in a viscous emulsion (Malipeddi & Sarkar 2019*b*) as can also be

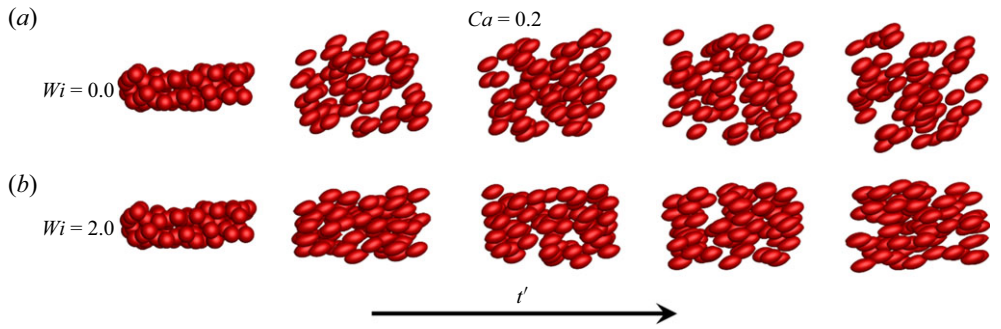

Figure 2. Spreading of drops in the velocity gradient direction at $Ca = 0.2$ for $Wi = 0.0$ (a) and $Wi = 2.0$ (b).

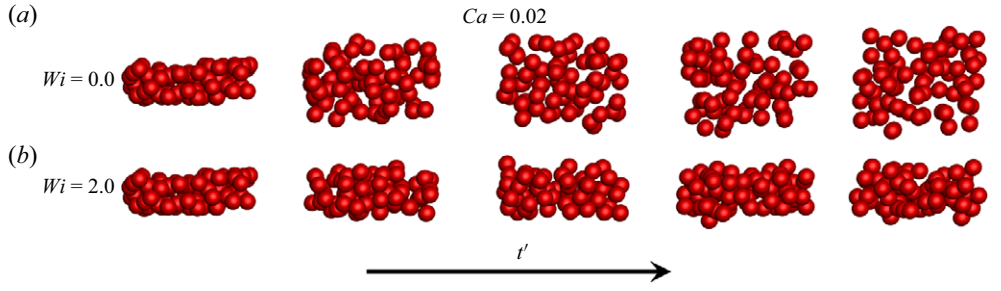

Figure 3. Spreading of drop emulsion in the velocity gradient direction at $Ca = 0.02$ for $Wi = 0.0$ (a) and $Wi = 2.0$ (b).

seen in figure 3. The lower Ca also further strengthens the viscoelastic effects, leading to near elimination of diffusion at higher $Wi = 2.0$. The thickness of the compact layer of drops nearly retains its original value, although drops are constantly interacting with each other, changing their positions. As discussed below, the decreased diffusion of drops with increasing viscoelasticity of the surrounding medium (more prominent at lower Ca) can be explained by our previous study of pair interaction between drops in a viscoelastic medium (Tarafder *et al.* 2022). It showed that surrounding viscoelasticity results in high extensional stresses between separating drops. Furthermore, the elastic tension around a drop created a larger region of spiralling streamlines, eventually trapping a second drop into tumbling trajectories at high Wi and low Ca values. These characteristics of pair interaction led to decreased separation between drops at low Ca and high Wi seen here.

In figures 4(a) and 4(b), we show the Taylor deformation $D = (L - B)/(L + B)$ (assuming approximately an ellipsoidal shape of the deformed drop; L and B are the major and minor axes, respectively) and inclination angle averaging over all drops for $Ca = 0.2$ and $Ca = 0.02$. They show a larger deformation and stronger alignment with the flow for the larger Ca, as expected. We also show that drop deformation and inclination angle decrease with Wi (also see Aggarwal & Sarkar 2007, 2008a). The noise in drop deformation and inclination angle indicates frequent interactions with neighbours. At higher Ca, we note a slightly increased drop deformation and alignment towards the flow at higher viscoelasticity, which may facilitate drops passing each other, thereby reducing the post-collision separation in the velocity gradient direction and the shear-induced diffusivity. On the other hand, at lower Ca, the drop deformation is small and

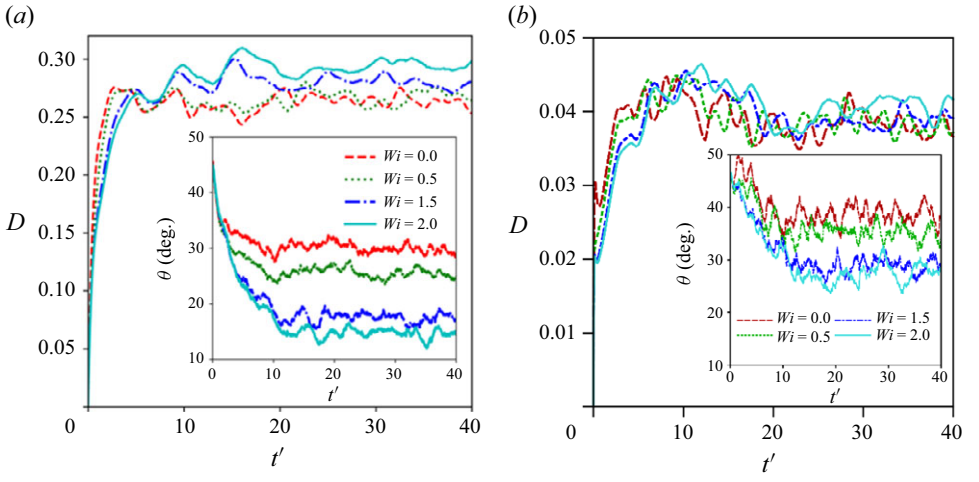

Figure 4. Average drop deformation and inclination angle for (*a*) $Ca = 0.2$, and (*b*) $Ca = 0.02$.

does not show significant dependence on Wi. Note that this is consistent with our earlier finding that, rather than drop shapes, the flow around them impacts the pair interaction in a viscoelastic medium; effects of viscoelasticity are maximal at lower Ca, where deformation is minimal. Rather than the deformability, the viscoelastic hindering of drop separation is the dominant effect in determining the diffusivity, indicating similar physics for rigid particles as well. Similar spiralling streamline patterns were seen around a rigid sphere in a viscoelastic fluid (D'Avino *et al.* 2008). Our previous pair-interaction study (Tarafder *et al.* 2022) also found hindered drop separation at an increased viscosity ratio, indicating reduced shear-induced diffusion in the limit of rigid spheres at an infinite viscosity ratio.

In figure 5, we plot drop positions vs. time, showing a random walk-like individual drop motion. At $Ca = 0.2$, for both $Wi = 0.0$ and $Wi = 2.0$, drop positions spread in the velocity gradient direction with time. However, for $Ca = 0.02$ and $Wi = 2.0$, the spreading is minimal, indicating no diffusion along the shear direction (as we have also seen in figure 3 bottom panel).

Figure 6 shows the concentration profile of the drop layer at three different times. Figures 6(*a*) and 6(*b*) show the cases when drops are more deformable, $Ca = 0.2$. For both $Wi = 0.0$ and 2.0, the parabolic concentration profile spreads with time, indicating collective diffusion, the spreading being lower for $Wi = 2.0$ compared with $Wi = 0.0$ due to increased drop deformation and resulting stronger alignment with the flow, in conformity with figure 5.

Figures 6(*c*) and 6(*d*) show the case for a low $Ca = 0.02$ when the drops are less deformable and nearly retain their spherical shape (figure 3). The concentration profiles of the drop layer at $Ca = 0.02$, $Wi = 0.0$ (viscous case) at different times are similar to the viscous case at $Ca = 0.2$ but with a slower spreading of the layer thickness (see also figure 5), i.e. lower diffusivity, also seen before (Malipeddi & Sarkar, 2019*b*). However, for the viscoelastic case ($Wi = 2.0$) (figure 6*d*), the concentration profile of the drops shows negligible change, indicating minimal diffusion at lower Ca and higher Wi as we saw in figures 3 and 5. In the insets of figure 6, we plot the concentration profile for each case using scaled variables showing approximate collapse of profiles from different

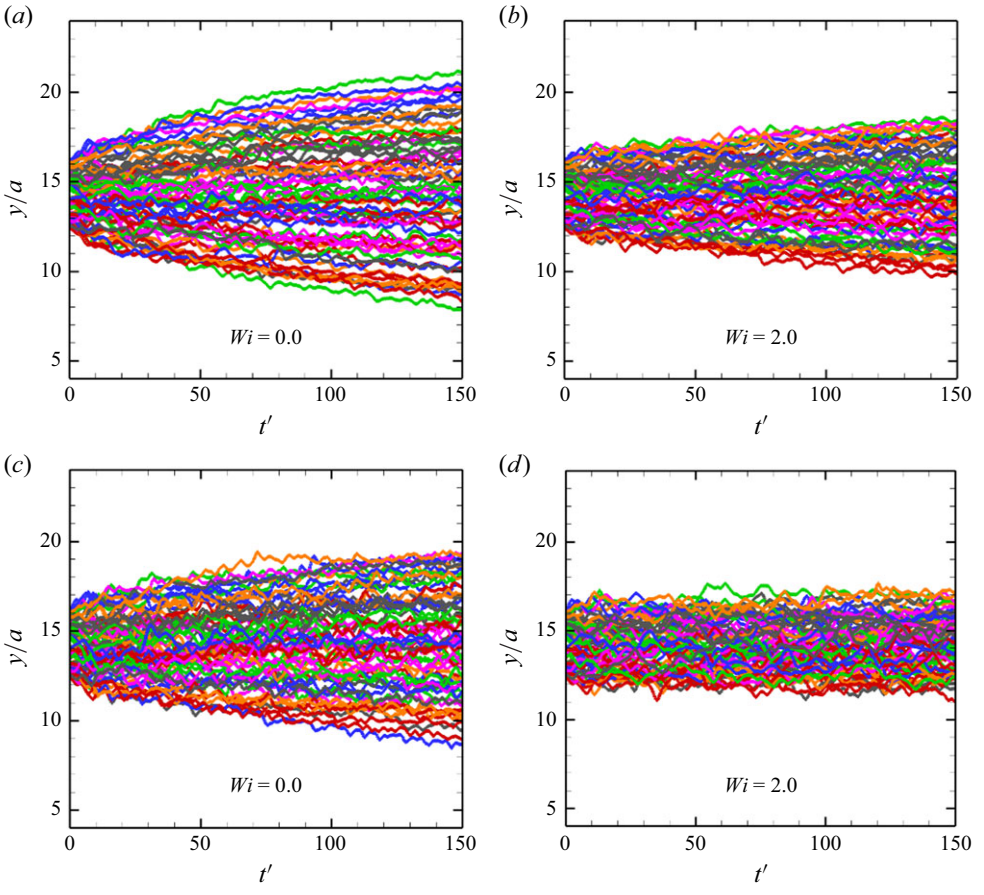

Figure 5. Drop position vs. time at $Ca = 0.2$ (*a*,*b*) and $Ca = 0.02$ (*c*,*d*) for viscous and viscoelastic cases.

time instants to a single curve, in conformity with (2.6), except for the low deformable ($Ca = 0.02$) high viscoelastic ($Wi = 2.0$) case (figure 6*d*). For this case, profiles from different time instants in the original (non-scaled) variables show little variation over time, indicating minimal diffusion. Therefore, scaling the variables with time rather than collapsing them to a single curve separates them.

As noted before, in our recent work (Tarafder *et al.* 2022) we have shown that increasing viscoelasticity of the surrounding fluid reduces post-collision separation of streamlines of passing drops, eventually trapping them in tumbling trajectories at low *Ca* and high *Wi*, where the drops do not separate but rotate around the centre of the line joining them. The transition from a passing to a tumbling trajectory was ascribed to the presence of a large region of spiralling streamlines around a single drop in a viscoelastic shear flow, which traps the approaching second drop. The hoop stress due to the first normal stress difference around the spherical drop (at lower *Ca*) generates the region of spiralling streamlines. We provided a perturbative theory for the effects of the first normal stress difference in determining the region of the spiralling streamlines that approximately explains the scaling of the critical *Ca* vs. *Wi* curve delineating the transition from passing to tumbling trajectories at low *Ca* and high *Wi*. We also showed that, during the separation

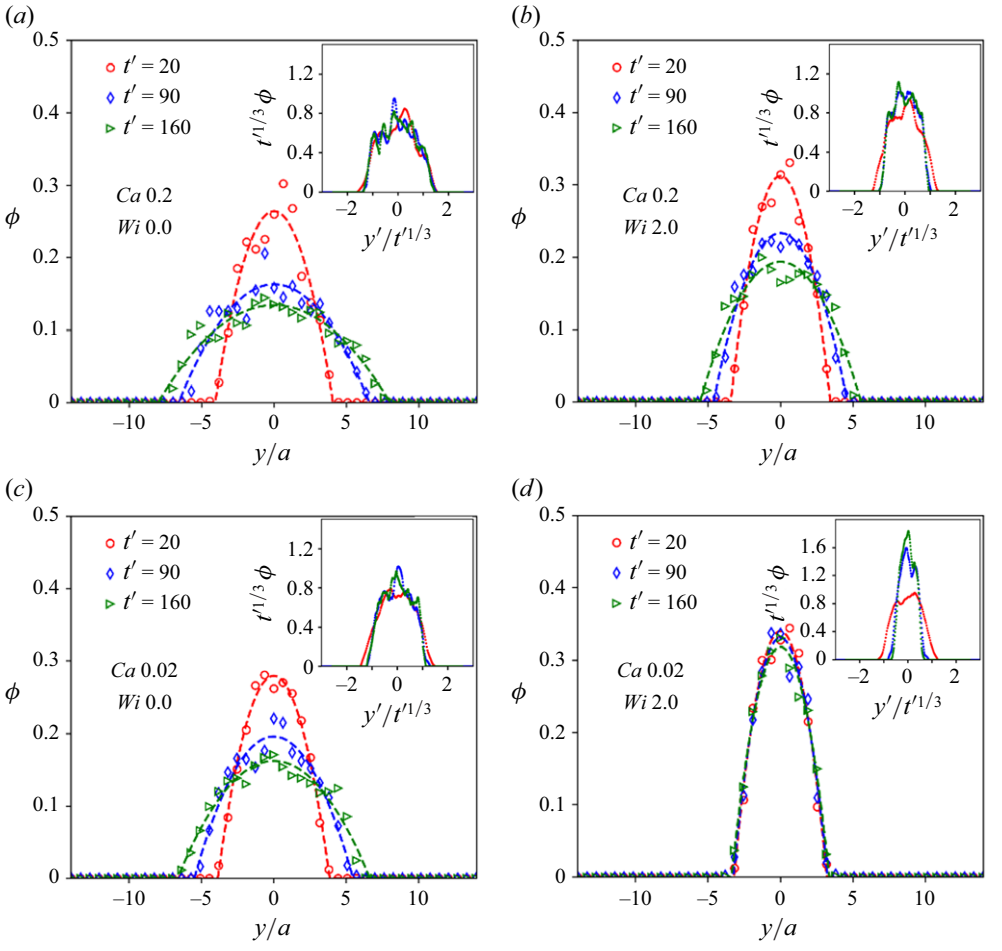

Figure 6. Concentration profile of drops at different non-dimensional times for $Ca = 0.2$ (*a, b*) and $Ca = 0.02$ (*c, d*) for viscous (*a, c*) and viscoelastic (*b, d*) cases. Lines are best-fitted parabolas. Insets show concentrations at the same time instants (same colours) scaled with $t^{1/3}$ (as per (2.6)) collapsing to a single curve due to self-similar evolution.

of interacting drops, high polymeric stresses develop in the separation quadrant, hindering their separation. The decreased separation between drops is the primary driving force hindering the shear-induced diffusion of drops seen here retaining their original compact configuration (figures 3*b*, 5*d*, 6*d*) and leading to almost zero spreading at this high *Wi* and low *Ca* case.

In figure 7, following (2.9), we plot the cube of the width of the concentration profile with time, $Ca = 0.2$ and $Ca = 0.02$ for different *Wi* values, showing the $t'^{1/3}$ scaling noted before (best fitted lines are shown). The rate of spreading indicated by the slope of the curves decreases with increasing *Wi* for both *Ca* values. For $Ca = 0.02$, the slope eventually goes to zero at $Wi = 2.0$, indicating zero diffusion. We calculate the collective diffusivity f_2 according to (2.9) from the slope and plot it in figure 8(*a*) for various *Ca* as a function of *Wi*. The fitted curves show an approximate linear scaling of f_2 with *Wi* for all the *Ca* values we have studied. The corresponding plot of f_2 with *Ca* for different *Wi* values is shown in figure 8(*b*). As noted in Tarafder *et al.* (2022), the effects of

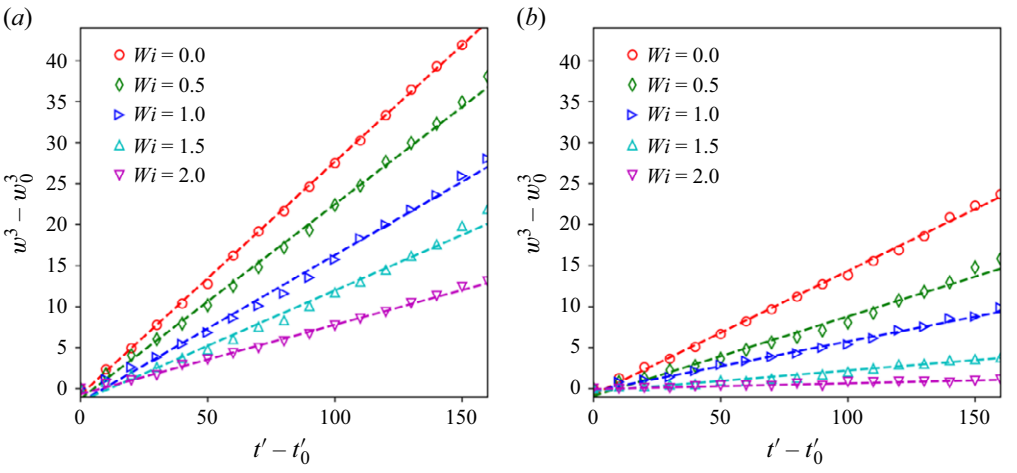

Figure 7. Width of drop layer as a function of time at $Ca = 0.2$ (a) and $Ca = 0.02$ (b) for different Wi' values.

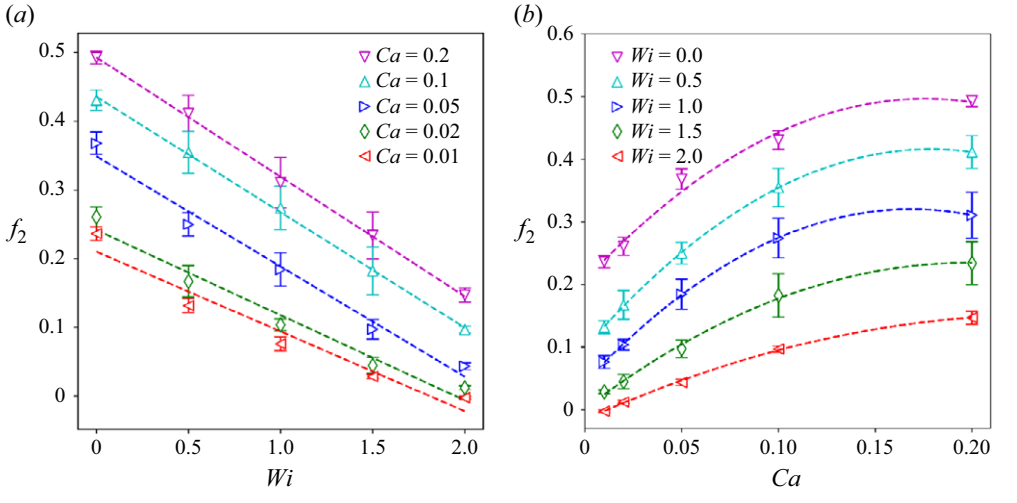

Figure 8. Collective diffusivity varying with Wi for various Ca (a) and varying with Ca for various Wi (b).

surrounding fluid viscoelasticity on pair interaction are complex, resulting from the flow field around the drops determined by the viscoelastic stresses competing with the imposed shear flow (Aggarwal & Sarkar, 2008*a*). The dynamics resulted in the emergent linear decay seen in figure 8(*a*) (Appendix briefly considers the effects of β showing that f_2 decays approximately linearly with $Wi\beta$). The non-monotonic variation of f_2 seen here with Ca for the viscous case ($Wi = 0$) was also noted in Malipeddi & Sarkar (2019*b*). The diffusion increases with increasing Ca initially due to increased deformation, but it decreases at higher Ca because of increased alignment with the flow direction, facilitating the sliding of drops. At higher Wi, this non-monotonicity is subdued by viscoelasticity.

After computing the collective diffusivity from the layer thickness, (2.8) and (2.9), we compute it using the dynamic structure factor, (2.12). It has been plotted as a function of

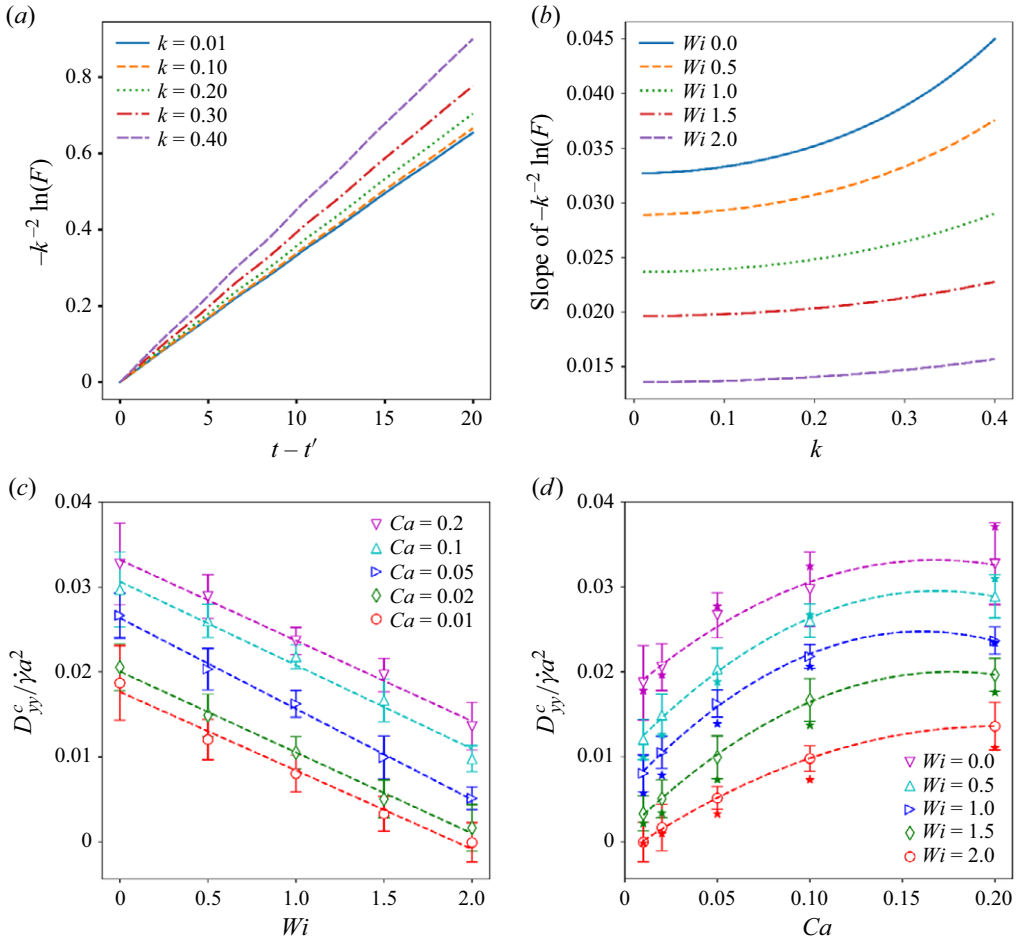

Figure 9. (*a*) Value of $-k^2 \ln F$ as a function of time for different k. (*b*) Slopes of curves in (*a*) for different Wi. (*c*) Value of D^c_{yy} vs. Wi for different Ca. (*d*) Value of D^c_{yy} vs. Ca for different Wi (the stars represent $0.0753 f_2$ for comparison).

time in figure 9(*a*) for different k at $Ca = 0.2$, showing linear growth with time, which tends to a common line as $k \to 0$. Figure 9(*b*) plots the slope of the curves in figure 9(*a*) for different Wi values, displaying a slow variation with wavenumber k, but reaching a limiting value D^c_{yy} as $k \to 0$, as we saw also for viscous cases (Malipeddi & Sarkar 2019*a*,*b*) and with red blood cells (Malipeddi & Sarkar 2021) (see the discussion in § 2). Figures 9(*c*) and 9(*d*) show that D^c_{yy} vs. Wi for different Ca values and D^c_{yy} vs. Ca for different Wi values show identical natures as f_2 plotted in figure 8. As noted before, the dynamic structure factor is typically applied to a homogeneous system of a certain (unchanging) volume fraction. There, the wavenumber-dependent gradient diffusivity is a property of the spontaneously appearing fluctuation at the length scale corresponding to that wavelength. Here, we computed the dynamic structure factor in a non-homogeneous system with continually changing volume fraction of the drop layer, preventing direct comparison with f_2. However, noting the relationship $D^c_{yy} = \dot{\gamma}\phi a^2 f_2$, we numerically find a fit $D^c_{yy}/\dot{\gamma}a^2 f_2 = \phi = 0.0753$ for an overall average volume fraction scale of ∼0.1

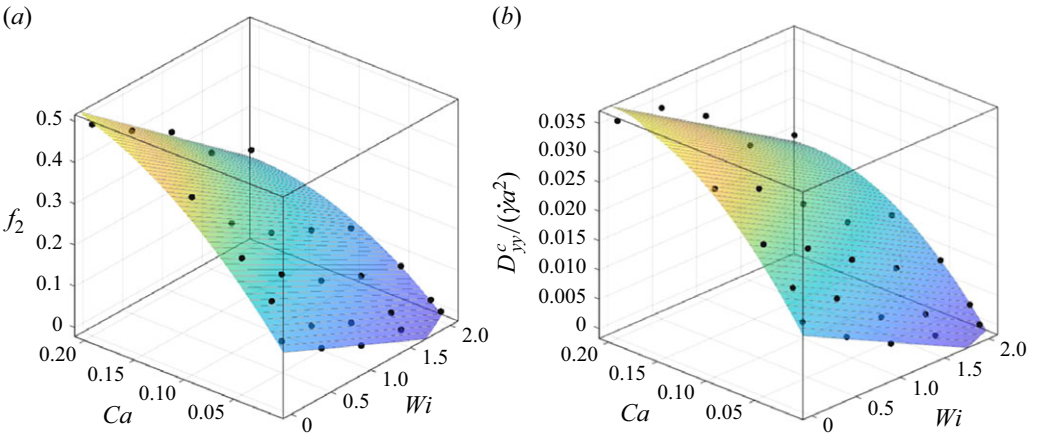

Figure 10. Variation of f_2 (*a*) and D^c_{yy} (*b*) as functions of *Ca* and *Wi*.

during the entire time evolution. It led to a good match between the two computations in figure 9(*d*).

Finally, figures 10(*a*) and 10(*b*) display surface plots of f_2 and D^c_{yy} as functions of *Wi* and *Ca* showing their identical nature. We also independently obtain curve fits for the surfaces of f_2 and D^c_{yy} in figures 10(*a*) and 10(*b*)

$$f_2 = 0.15 - 0.1Wi + 3.25Ca - 0.25WiCa - 7.35Ca^2,$$
$$D^c_{yy}/\dot{\gamma}a^2 = 0.014 - 0.008Wi + 0.22Ca - 0.002WiCa - 0.6Ca^2. \quad (3.1)$$

These relations are approximately consistent with the volume fraction scale $D^c_{yy}/\dot{\gamma}a^2 f_2 = \phi \sim 0.1$ used before in figure 9(*d*). Note that such correlations as in the viscous cases (Malipeddi & Sarkar 2019*a*,*b*) are purely phenomenological and are based on the computed diffusivities in the study and are therefore not applicable outside the range of parameters of that study. Nonetheless, the correlation here is approximately close to the viscous case in the limit of $Wi = 0$. In Appendix, we briefly consider the effects of β variation away from the value of 0.5 studied here.

4. Conclusion

Following our previous investigation of shear-induced gradient/collective diffusion of viscous drops and red blood cells in viscous media, here, we investigate the effects of viscoelasticity of the surrounding medium. As before, we use a front-tracking finite difference method to simulate a compact layer of viscous drops in a shear flow, which presents a sharp concentration gradient at the layer boundary. The surrounding fluid is modelled using a FENE-type constitutive equation. The drops undergo shear-induced collective diffusion because of the concentration gradient and spread in the velocity gradient direction. The diffusivity is computed using a one-third scaling of the layer width with time as well as an independent means of a dynamic structure factor approach, both methods resulting in matching results.

In a viscoelastic fluid, drops spread less, eventually leading to zero diffusion at low capillary numbers and high Weissenberg numbers. The physics underlying the reduced diffusion stems from the specific nature of pair interaction in a viscoelastic fluid flow recently investigated (Tarafder *et al.* 2022). Fluid viscoelasticity due to polymeric stresses

changes the local flow field near a drop in a shear flow, hindering post-collision drop-separation. At higher *Wi* and lower *Ca*, tension along streamlines around a spherical drop creates a region of spiralling streamlines, eventually transitioning a passing trajectory of drops into a tumbling one where the drops revolve around each other. As a result of this hindered separation, the drop layer experiences reduced dispersion in the velocity gradient direction. Shear-induced diffusivity shows a linear decrease with *Wi*. Appendix briefly considers the effects of the ratio of polymeric viscosity to the total viscosity β to show that increasing it further enhances the effects of viscoelasticity.

Shear-induced diffusion is an important factor in industrial flows for enhancing mixing as well as in microfluidic particle technologies such as particle separation and flow focusing. This investigation indicates the possibility of using viscoelasticity as an additional means to control particulate flows in these applications. The range of capillary numbers (0.01–0.2) studied here aligns well with past experimental observations and industrial applications involving non-breaking drops. However, Weissenberg number varies widely in practice depending on the fluid chosen. The current study is limited to $Wi \leq 2.0$, which is sufficient for the current aim to explore the effects of viscoelasticity on diffusion. The current study is limited to monodisperse viscosity-matched drops in a non-shear-thinning Boger-type viscoelastic fluid. However, we note that our pair-interaction study (Tarafder *et al.* 2022) has shown that increasing the viscosity ratio enhances viscoelastic hindering of drop separation. It indicates that on increasing the viscosity ratio in an emulsion, as well as in its infinite limit, a rigid suspension of rigid particles would experience similar physics and a reduced shear-induced gradient diffusion. This study adequately demonstrates the first-order effects of the matrix viscoelasticity on the diffusion of suspended drops. Future work may consider bi/polydisperse emulsions common in many industrial flows.

Funding. K.S. acknowledges partial support from the National Science Foundation Award 1239105.

Declaration of interests. The authors declare no competing interests.

Author contributions. A.T. and K.S. conceptualised the problem. A.T. and A.R. performed the computations. A.T., A.R. and K.S. contributed to analysing the data, reaching the conclusion, and writing the manuscript. K.S. and A.R. revised the manuscript. K.S. supervised the overall project.

Data availability. The data sets generated and/or analysed during the current study are available from the corresponding author upon reasonable request.

Appendix Effects of β variation

In the interest of brevity and a reasonable computational time for the entire study, we varied only *Ca* and *Wi* to investigate their effects on the shear-induced gradient diffusivity, keeping all other parameters fixed, including $\beta = 0.5$. In this appendix, we briefly consider the effects of β variation on f_2. Figure 11(*a*) plots f_2 for three different values of β. We note that, except for the lowest value $\beta = 0.1$, where the diffusivity values are very close to the viscous case, the others show an approximately linear decreasing trend with β similar to the variation with *Wi*. Note that β signifies the amount of polymer viscosity and the first normal stress difference in the viscoelastic medium is $N_1 = 2\lambda\mu_p\dot{\gamma}^2$ with its non-dimensionalised counterpart $N_1/\mu\dot{\gamma} = 2Wi\beta$. Previously, we found that, for the single drop dynamics in shear, the deformation and inclination for different β values collapsed to one curve when plotted against $Wi\beta$ (Aggarwal & Sarkar, 2007, 2008*a*). Figure 11(*b*) also shows that f_2 approximately decreases linearly with this quantity.

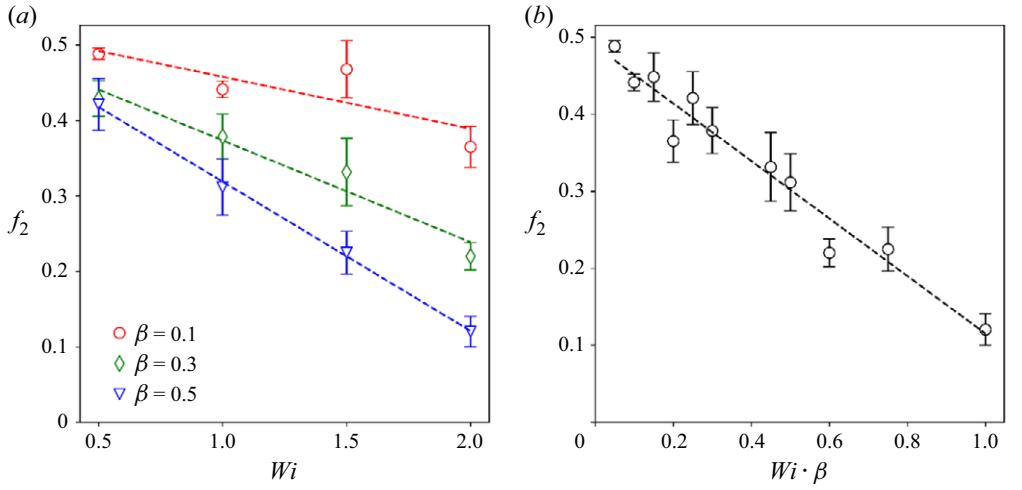

Figure 11. Variation of f_2 vs. Wi (*a*) and f_2 vs. $Wi\beta$ (*b*) for $Ca = 0.2$.

References

Acrivos, A. 1995 BINGHAM AWARD LECTURE—1994 shear-induced particle diffusion in concentrated suspensions of noncolloidal particles. *J. Rheol.* **39** (5), 813–826.

Aggarwal, N. & Sarkar, K. 2007 Deformation and breakup of a viscoelastic drop in a Newtonian matrix under steady shear. *J. Fluid Mech.* **584**, 1–21.

Aggarwal, N. & Sarkar, K. 2008*a* Effects of matrix viscoelasticity on viscous and viscoelastic drop deformation in a shear flow. *J. Fluid Mech.* **601**, 63–84.

Aggarwal, N. & Sarkar, K. 2008*b* Rheology of an emulsion of viscoelastic drops in steady shear. *J. Non Newtonian Fluid Mech.* **150** (1), 19–31.

Chilcott, M.D. & Rallison, J.M. 1988 Creeping flow of dilute polymer solutions past cylinders and spheres. *J. Non-Newtonian Fluid Mech.* **29**, 381.

Choi, Y.J. & Hulsen, M.A. 2012 Alignment of particles in a confined shear flow of a viscoelastic fluid. *J. Non-Newtonian Fluid Mech.* **175**, 89–103.

D'Avino, G., Hulsen, M.A., Snijkers, F., Vermant, J., Greco, F. & Maffettone, P.L. 2008 'Rotation of a sphere in a viscoelastic liquid subjected to shear flow Part I: Simulation results'. *J. Rheol.* **52** (6), 1331–1346.

Da Cunha, F.R. & Hinch, E.J. 1996 Shear-induced dispersion in a dilute suspension of rough spheres. *J. Fluid Mech.* **309**, 211–223.

Dou, H.-S. & Phan-Thien, N. 2003 Negative wake in the uniform flow past a cylinder. *Rheol. Acta* **42** (5), 383.

Eckstein, E.C., Bailey, D.G. & Shapiro, A.H. 1977 Self-diffusion of particles in shear flow of a suspension. *J. Fluid Mech.* **79** (01), 191–208.

Grandchamp, X., Coupier, G., Srivastav, A., Minetti, C. & Podgorski, T. 2013 Lift and down-gradient shear-induced diffusion in red blood cell suspensions. *Phys. Rev. Lett.* **110** (10), 108101.

Hudson, S.D. 2003 Wall migration and shear-induced diffusion of fluid droplets in emulsions. *Phys. Fluids* **15** (5), 1106–1113.

Izbassarov, D. & Muradoglu, M. 2015 A front-tracking method for computational modeling of viscoelastic two-phase flow systems. *J. Non-Newtonian Fluid Mech.* **223**, 122–140.

Jaensson, N.O., Hulsen, M.A. & Anderson, P.D. 2016 Direct numerical simulation of particle alignment in viscoelastic fluids. *J. Non-Newtonian Fluid Mech.* **235**, 125–142.

Kim, J.M., Kim, C., Chung, C., Ahn, K.H. & Lee, S.J. 2005 Negative wake generation of FENE-CR fluids in uniform and Poiseuille flows past a cylinder. *Rheol. Acta* **44** (6), 600.

Kim, S., Han, M. & Kim, C. 2000 Hydrodynamic diffusivity of spherical particles in polymer solution. *Rheol. Acta* **39** (5), 495–502.

King, M.R. & Leighton, D.T. 2001 Measurement of shear-induced dispersion in a dilute emulsion. *Phys. Fluids* **13** (2), 397–406.

KOH, C.J., HOOKHAM, P. & LEAL, L.G. 1994 An experimental investigation of concentrated suspension flows in a rectangular channel. *J. Fluid Mech.* **266**, 1–32.
KULKARNI, P.M. & MORRIS, J.F. 2008 Pair-sphere trajectories in finite-Reynolds-number shear flow. *J. Fluid Mech.* **596**, 413–435.
LEIGHTON, D. & ACRIVOS, A. 1987 The shear-induced migration of particles in concentrated suspensions. *J. Fluid Mech.* **181**, 415–439.
LESHANSKY, A.M. & BRADY, J.F. 2005 Dynamic structure factor study of diffusion in strongly sheared suspensions. *J. Fluid Mech.* **527**, 141–169.
LESHANSKY, A.M., MORRIS, J.F. & BRADY, J.F. 2008 Collective diffusion in sheared colloidal suspensions. *J. Fluid Mech.* **597**, 305–341.
LI, X. & SARKAR, K. 2005 Drop dynamics in an oscillating extensional flow at finite Reynolds numbers. *Phys. Fluids* **17** (2), 027103.
LOEWENBERG, M. & HINCH, E.J. 1997 Collision of two deformable drops in shear flow. *J. Fluid Mech.* **338**, 299–315.
LOPEZ, M. & GRAHAM, M.D. 2008 Enhancement of mixing and adsorption in microfluidic devices by shear-induced diffusion and topography-induced secondary flow. *Phys. Fluids* **20**, 053304.
MALIPEDDI, A.R. & SARKAR, K. 2019*a* Collective diffusivity in a sheared viscous emulsion: effects of viscosity ratio. *Phys. Rev. Fluids* **4** (9), 093603.
MALIPEDDI, A.R. & SARKAR, K. 2019*b* Shear-induced collective diffusivity down a concentration gradient in a viscous emulsion of drops. *J. Fluid Mech.* **868**, 5–25.
MALIPEDDI, A.R. & SARKAR, K. 2021 Shear-induced gradient diffusivity of a red blood cell suspension: effects of cell dynamics from tumbling to tank-treading. *Soft Matt.* **17**, 8523–8535.
MARCHIORO, M. & ACRIVOS, A. 2001 Shear-induced particle diffusivities from numerical simulations. *J. Fluid Mech.* **443**, 101–128.
MATOS, H.M., ALVES, M.A. & OLIVEIRA, P.J. 2009 New formulation for stress calculation: application to viscoelastic flow in a T-junction. *Numer. Heat Transfer Part B: Fundam.* **56** (5), 351.
MORRIS, J.F. & BRADY, J.F. 1996 Self-diffusion in sheared suspensions. *J. Fluid Mech.* **312**, 223–252.
MUKHERJEE, S. & SARKAR, K. 2009 Effects of viscosity ratio on deformation of a viscoelastic drop in a Newtonian matrix under steady shear. *J. Non-Newtonian Fluid Mech.* **160**, 104–112.
MUKHERJEE, S. & SARKAR, K. 2010 Effects of viscoelasticity on the retraction of a sheared drop. *J. Non-Newtonian Fluid Mech.* **165** (7–8), 340–349.
MUKHERJEE, S. & SARKAR, K. 2011 Viscoelastic drop falling through a viscous medium. *Phys. Fluids* **23**, 013101.
MUKHERJEE, S. & SARKAR, K. 2013 Effects of matrix viscoelasticity on the lateral migration of a deformable drop in a wall-bounded shear. *J. Fluid Mech.* **727**, 318–345.
MUKHERJEE, S. & SARKAR, K. 2014 Lateral migration of a viscoelastic drop in a Newtonian fluid in a shear flow near a wall. *Phys. Fluids* **26**, 103102.
MUKHERJEE, S., TARAFDER, A., MALIPEDDI, A.R. & SARKAR, K. 2022 Shear-induced migration of a viscous drop in a viscoelastic liquid near a wall at high viscosity ratio: reverse migration. *J. Non-Newtonian Fluid Mech.* **301**, 104751.
OLIVEIRA, P.J. 2003 Asymmetric flows of viscoelastic fluids in symmetric planar expansion geometries. *J. Non-Newtonian Fluid Mech.* **114** (1), 33–63.
PASQUINO, R., PANARIELLO, D. & GRIZZUTI, N. 2013 Migration and alignment of spherical particles in sheared viscoelastic suspensions. A quantitative determination of the flow-induced self-assembly kinetics. *J. Colloid Interface Sci.* **394**, 49–54.
RALLISON, J.M. & HINCH, E.J. 1986 The effect of particle interactions on dynamic light scattering from a dilute suspension. *J. Fluid Mech.* **167**, 131–168.
RAMACHANDRAN, A., LOEWENBERG, M. & LEIGHTON, D.T. 2010 A constitutive equation for droplet distribution in unidirectional flows of dilute emulsions for low capillary numbers. *Phys. Fluids* **22** (8), 083301.
RAMASWAMY, S. & LEAL, L.G. 1999 The deformation of a viscoelastic drop subjected to steady uniaxial extensional flow of a Newtonian fluid. *J. Non-Newtonian Fluid Mech.* **85** (2–3), 127–163.
ROURE, G.A. & CUNHA, F.R. 2018 Hydrodynamic dispersion and aggregation induced by shear in non-Brownian magnetic suspensions. *Phys. Fluids* **30** (12), 122002.
SARKAR, K. & SCHOWALTER, W.R. 2000 Deformation of a two-dimensional viscoelastic drop at non-zero Reynolds number in time-periodic extensional flows. *J. Non-Newtonian Fluid Mech.* **95** (2–3), 315–342.
SCIROCCO, R., VERMANT, J. & MEWIS, J. 2004 Effect of the viscoelasticity of the suspending fluid on structure formation in suspensions. *J. Non-Newtonian Fluid Mech.* **117** (2–3), 183–192.

SNIJKERS, F., PASQUINO, R. & VERMANT, J. 2013 Hydrodynamic interactions between two equally sized spheres in viscoelastic fluids in shear flow. *Langmuir* **29** (19), 5701–5713.

SRIVASTAVA, P., MALIPEDDI, A.R. & SARKAR, K. 2016 Steady shear rheology of a viscous emulsion in the presence of finite inertia at moderate volume fractions: sign reversal of normal stress differences. *J. Fluid Mech.* **805**, 494–522.

SZABO, P., RALLISON, J.M. & HINCH, E.J. 1997 Start-up of flow of a FENE-fluid through a 4: 1: 4 constriction in a tube. *J. Non-Newtonian Fluid Mech.* **72** (1), 73.

TARAFDER, A., MALIPEDDI, A.R. & SARKAR, K. 2022 Pair interactions between viscous drops in a viscoelastic matrix in free shear: transition from passing to tumbling trajectories. *J. Rheol.* **66** (3), 571–584.

WON, D. & KIM, C. 2004 Alignment and aggregation of spherical particles in viscoelastic fluid under shear flow. *J. Non-Newtonian Fluid Mech.* **117** (2–3), 141–146.

ZENIT, R. & FENG, J.J. 2018 Hydrodynamic interactions among bubbles, drops, and particles in non-Newtonian liquids. *Annu. Rev. Fluid Mech.* **50**, 505–534.

ZHOU, J. & PAPAUTSKY, I. 2019 Size-dependent enrichment of leukocytes from undiluted whole blood using shear-induced diffusion. *Lab on a Chip* **19** (20), 3416–3426.

ZHOU, J. & PAPAUTSKY, I. 2020 Viscoelastic microfluidics: progress and challanges. *Microsyst. Nanoengng* **6** (1), 1–24.

ZHOU, J., TU, C., LIANG, Y., HUANG, B., FANG, Y., LIANG, X., PAPAUTSKY, I. & YE, X. 2018 Isolation of cells from whole blood using shear-induced diffusion. *Sci. Rep.* **8** (1), 9411.